scientific reports

Check for updates

OPEN

Noninvasive PET imaging of LPS-induced oxidative stress in skeletal muscle using a ROS-targeting radiotracer

Joo Yeon Park[1,4], Sun Mi Park[1,4], Tae Sup Lee[2], Sang Ju Lee[3], Ji-Young Kim[1], Seung Jun Oh[3], Hai-Jeon Yoon[1], Bom Sahn Kim[1]✉ & Byung Seok Moon[1]✉

Skeletal muscle atrophy is characterized by the progressive loss of muscle mass and function, driven by multifactorial processes such as inflammation, mitochondrial dysfunction, and oxidative stress. Among these mechanisms, excessive generation of reactive oxygen species (ROS) represents a central pathogenic event that disrupts redox homeostasis and contributes to muscle degeneration. In this study, we primarily aimed to the feasibility of using the ROS-targeted PET radiotracer, [^{18}F] ROStrace, as a non-invasive imaging tool for visualizing ROS accumulation in skeletal muscle. The association between [^{18}F]ROStrace uptake and molecular or histological changes related to oxidative stress and atrophy was analyzed to biologically validate the imaging signal. Cellular uptake of [^{18}F] ROStrace increased in a time-dependent manner in LPS-treated myotubes, reaching 18.0 ± 3.4%ID at 120 min. Uptake was significantly higher in LPS-treated myotubes (9.7 ± 0.4%ID) compared to antioxidant-pretreated cells (7.2 ± 0.4%ID, *N*-acetylcysteine), while oxidative stress-enhanced cells (piperlongumine-pretreated cells, 10.1 ± 1.3%ID) showed similar uptake to the LPS group. In vivo, LPS-treated mice exhibited markedly increased [^{18}F]ROStrace uptake in hindlimb muscles compared to controls (2.2 ± 0.3 vs. 0.9 ± 0.2%ID/g, $p < 0.001$), reflecting elevated oxidative burden. The PET signal was associated with molecular and histological markers of redox imbalance, including upregulation of MuRF-1 and Atrogin-1 mRNA (~ 13-fold and ~ 10-fold, respectively), reduced muscle fiber cross-sectional area, and a two-fold increase in dihydroethidium (DHE) fluorescence. Collectively, these findings demonstrate that [^{18}F]ROStrace PET imaging enables sensitive, in vivo assessment of oxidative stress in skeletal muscle, providing a foundation for early diagnosis and therapeutic monitoring of redox-associated muscle disorders.

Keywords Skeletal muscle, ROS imaging, oxidative stress, positron emission tomography, [^{18}F]ROStrace

Skeletal muscle atrophy, defined as the progressive decline in muscle mass and strength, results from complex molecular mechanisms including inflammation, mitochondrial dysfunction, and oxidative stress[1–9]. Among these, oxidative stress plays an central role by generating excessive reactive oxygen species (ROS) that disrupt cellular redox balance, impair mitochondrial function, and activate proteolytic signaling[10–15]. Importantly, ROS elevation precedes structural loss, representing an early biochemical signature of muscle degeneration rather than atrophy itself.

Prolonged oxidative stress accelerates muscle protein breakdown through activation of the ubiquitin–proteasome system (UPS), leading to upregulation of the E3 ligases MuRF-1 and Atrogin-1, hallmark markers of muscle wasting[14–17]. Concurrently, mitochondrial dysfunction and redox-sensitive transcriptional pathways such as NF-κB and MAPK amplify inflammatory signaling and compromise muscle regeneration[15,18–21]. While these biological processes provide mechanistic context, they are distinct from the primary objective of the present study, which is to visualize ROS generation directly in skeletal muscle using PET imaging.

[1]Department of Nuclear Medicine, Ewha Womans University College of Medicine, Seoul 07804, South Korea. [2]Division of RI Applications, Korea Institute Radiological and Medical Sciences, Seoul 01812, South Korea. [3]Department of Nuclear Medicine, Asan Medical Center, University of Ulsan College of Medicine, Seoul 05505, South Korea. [4]Joo Yeon Park and Sun Mi Park contributed equally to this work. ✉email: kbomsahn@ewha.ac.kr; bsmoon@ewha.ac.kr

Current diagnostic approaches, including biopsy, MRI, and CT, can detect morphological or volumetric changes but fail to capture oxidative stress in vivo[7]. In contrast, positron emission tomography (PET) with ROS-sensitive radiotracers allows quantitative visualization of redox dynamics at the molecular level[22–26]. Such imaging provides a mechanistic window into oxidative injury before overt muscle loss, offering potential for early detection and therapeutic evaluation.

Several ROS-targeted probes have been developed to detect specific species such as superoxide and hydrogen peroxide[18,19]. Among them, [^{18}F]ROStrace—a dihydroethidium-based radiotracer—demonstrates high selectivity for superoxide, favorable in vivo kinetics, and reproducible synthesis[27–30]. Compared with other radiotracers, it provides superior stability and low background in normal muscle, enhancing contrast for redox imaging.

In the present study, we investigated the feasibility of [^{18}F]ROStrace PET as a non-invasive imaging tool to visualize ROS accumulation in skeletal muscle, using a lipopolysaccharide (LPS)-induced murine model to mimic oxidative conditions associated with skeletal muscle inflammation and early atrophy gene expression. Both In vitro and in vivo experiments were designed to confirm that the observed [^{18}F]ROStrace signal reflects ROS generation, with mitochondrial and molecular indices serving as supportive validation.

Results

Radiochemistry

The ROS-targeting radiotracer [^{18}F]ROStrace was synthesized via nucleophilic aliphatic substitution of a tosylate precursor (2-(4-(3,8-bis((*tert*-butoxycarbonyl)amino)-5-methyl-5,6-dihydrophenanthridin-6-yl)phenoxy)ethyl 4-methylbenzenesulfonate) using [^{18}F]fluoride and tetrabutylammonium as a phase-transfer catalyst. The non-decay-corrected radiochemical yield, based on the radioactivity trapped on the QMA cartridge, was 13.6 ± 4.9% (n = 22). The radiochemical purity exceeded 99% as determined by analytical HPLC (UV absorbance at 254 nm). The molar activity (A_m) was 129 ± 42 GBq/μmol at the end of synthesis. The entire synthesis process was completed within 107.0 ± 6.2 min on average (Table 1). In the present system, the oxidized form, *ox*-[^{18}F]ROStrace, was produced as the predominant product after labeling and was efficiently reduced to [^{18}F]ROStrace using $NaBH_4$[27,29]. The resulting tracer remained stable (> 98% at 3 h post–end of synthesis) when stored in a refrigerator with ascorbic acid under light-protected conditions.

Cellular uptake of [^{18}F]ROStrace in differentiated C2C12 myotubes

The time-dependent uptake of [^{18}F]ROStrace was evaluated in differentiated C2C12 myotubes. Cells were incubated with approximately 10 μCi of [^{18}F]ROStrace per well for 10, 30, 60, and 120 min, and intracellular radioactivity was quantified using a gamma counter. [^{18}F]ROStrace uptake increased progressively with incubation time, with measured uptake values of 3.6 ± 1.4, 4.9 ± 0.5, 9.7 ± 0.4, and 18.0 ± 3.4%ID at 10, 30, 60, and 120 min, respectively (n = 5 per time point; Fig. 1A). To assess redox responsiveness of [^{18}F]ROStrace, additional groups were analyzed at 60 min post-incubation, where tracer uptake most clearly reflects intracellular ROS levels rather than structural or metabolic alterations. LPS-treated myotubes exhibited significantly higher uptake of [^{18}F]ROStrace (9.7 ± 0.4%ID, n = 5) compared to untreated control myotubes (7.1 ± 1.0%ID, n = 5). Pretreatment with the ROS scavenger, *N*-acetylcysteine (NAC; 3 mM) reduced uptake to 7.2 ± 0.4%ID, confirming the redox sensitivity of [^{18}F]ROStrace. In contrast, piperlongumine (PL; 10 μM), a ROS enhancer, further increased uptake to 10.1 ± 1.3%ID, comparable to or slightly higher than that of the LPS group (Fig. 1B). These findings consistently support that [^{18}F]ROStrace accumulation reflects intracellular ROS levels in a concentration-dependent manner.

Confirmation of biological and structural changes associated with LPS-induced oxidative stress in an in vitro skeletal muscle model

To establish an in vitro skeletal muscle model of LPS-induced oxidative stress, C2C12 myoblasts were differentiated into myotubes and treated with LPS (0.2 mg/mL) for 24 h. Morphological evaluation revealed

	Specification	[^{18}F]ROStrace
Radiochemical yield (%, n.d.c.)	N/A	13.6 ± 4.9
Radiochemical Purity (%)	> 95%	> 99%
Molar activity (GBq/μmol) at EOS	> 37	129 ± 42
Visual inspection	Clear, colorless, no precipitate	Passes
pH	4.0–8.0	5.5-7.0
Radionuclide identity	105–115 min	Passes
	0.511 and 1.02 MeV	Passes
Residual solvent analysis	Methanol (< 3000 ppm)	ND
	Acetonitrile (< 410 ppm)	ND
	Ethanol (< 10%, v/v)	6.22 ± 1.51 (max 7.41)
Endotoxins	< 175 EU/V	< 1.0 EU/mL
Stability at 2–8 °C	3 h from EOS (w/ aa)	> 98%

Table 1. Summary for production results. n.d.c., no-decay corrected; ND, not detected; w/ aa, with ascorbic acid.

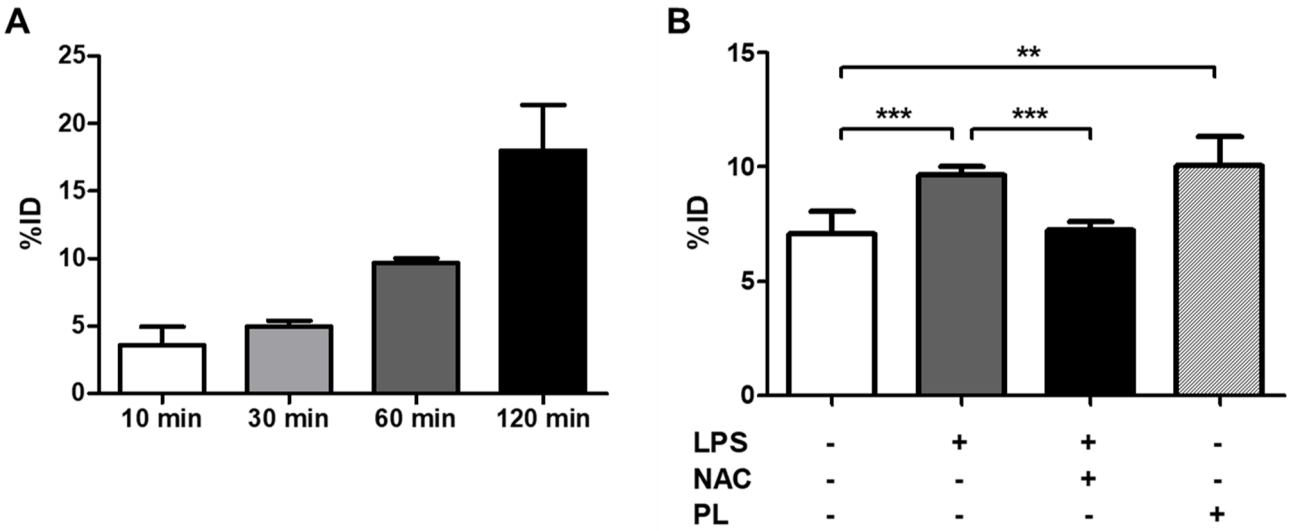


Fig. 1. [^{18}F]ROStrace uptake in C2C12 myotubes under oxidative stress conditions. (**a**) Time-dependent uptake of [^{18}F]ROStrace in LPS-treated C2C12 myotubes. Cells were incubated with the tracer for 10, 30, 60, and 120 min, and intracellular radioactivity was measured using a gamma counter ($n = 5$ per time point). Uptake is expressed as the percentage of the injected dose per well (%ID). (**b**) Comparative uptake of [^{18}F] ROStrace after 60 min of incubation in C2C12 myotubes treated with LPS (0.2 mg/mL), or pretreated with *N*-acetylcysteine (NAC, 3 mM) or piperlongumine (PL, 10 µM). LPS-treated myotubes showed significantly higher uptake than untreated controls ($p = 0.0005$, Cohen's $d = 3.54$, 95% CI [−3.627, −1.509]), while NAC pretreatment reduced tracer uptake ($p < 0.0001$, Cohen's $d = 6.51$, 95% CI [1.886, 2.974]). PL pretreatment resulted in significantly elevated uptake compared to untreated controls group ($p = 0.0051$, Cohen's $d = 2.54$, 95% CI [−4.707, −1.217]). Data are presented as mean ± standard deviation (SD); $n = 5$ for all groups.

marked structural changes in the LPS-treated myotubes compared to untreated controls (Fig. 2A). Quantitative analysis showed that the average myotube width was significantly reduced in the LPS-treated group (13.7 ± 2.4 µm) compared to the control group (19.3 ± 0.5 µm, $n = 3$), indicating atrophic features (Fig. 2B). To assess mitochondrial function, cells were stained with MitoTracker Red CMXRos and fluorescence intensity was analyzed (Fig. 2C). Compared to myoblasts, differentiated myotubes showed a 1.5-fold increase in fluorescence intensity (153.8 ± 6.5%), suggesting increased mitochondrial membrane potential. However, LPS-treated myotubes exhibited a significantly reduced MitoTracker fluorescence signal (119.1 ± 10.9%, $n = 3$), indicating a decrease in mitochondrial membrane potential (ΔΨm) under oxidative stress conditions (Fig. 2D). This reduction reflects altered mitochondrial polarization consistent with increased oxidative burden but does not by itself confirm mitochondrial dysfunction or atrophic change. This alteration in ΔΨm was used to biologically validate oxidative stress induction. Additionally, RT-qPCR analysis demonstrated that the mRNA expression levels of muscle atrophy-related genes, MuRF-1 and Atrogin-1, were significantly elevated following LPS treatment. MuRF-1 expression increased by 1.5-fold and Atrogin-1 by 1.2-fold compared to untreated controls ($n = 3$, $p < 0.05$; Fig. 2E).

Assessment of ROS accumulation in LPS-treated myotubes using DHE fluorescence

To confirm whether the oxidative stress detected by [^{18}F]ROStrace corresponded to increased ROS levels measured by a conventional ROS indicator, dihydroethidium (DHE) staining was performed in the in vitro model. C2C12 myotubes were incubated with 20 µM DHE for 30 min, and fluorescence images were acquired using a fluorescence microscope (Fig. 3A). Quantitative analysis revealed that the LPS-treated group exhibited a 1.9-fold increase in DHE fluorescence intensity (167.5 ± 70.9%) compared to the control group ($n = 9$). The difference was statistically significant, showing a marked increase (Fig. 3B).

PET analysis of [^{18}F]ROStrace uptake in an in vivo skeletal muscle model of LPS-induced oxidative stress

A 90-minute dynamic PET scan was performed to evaluate [^{18}F]ROStrace kinetics in control mice and low-dose LPS-induced oxidative stress mice (1 mg/kg; $n = 3$ per group). A lower LPS dose (1 mg/kg) was used during dynamic PET acquisition to ensure physiological stability under prolonged anesthesia, as higher doses (e.g., 5 mg/kg) occasionally caused severe systemic responses during the 90-minute scan. The 1 mg/kg dose was sufficient to induce a mild inflammatory response, allowing assessment of tracer kinetics under stable imaging conditions. Time-activity curves (TACs) were generated from regions of interest in the hindlimb muscles (Fig. 4). Both groups showed a rapid increase in tracer uptake during the initial phase, followed by a plateau. Steady-state uptake was observed between 60 and 80 min post-injection, indicating an optimal window for static PET imaging in this model.

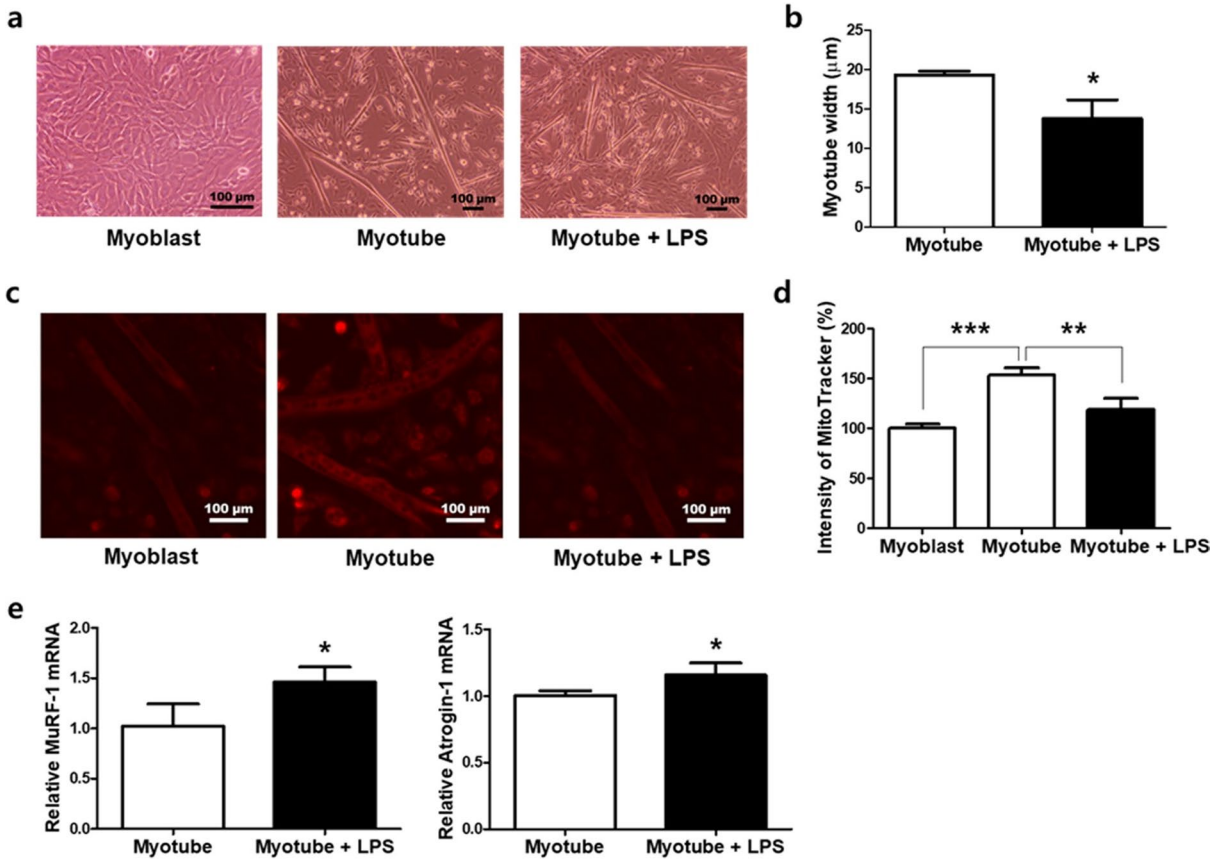


Fig. 2. Biological and structural alterations in LPS-treated C2C12 myotubes. (**a**) Representative phase-contrast images of C2C12 myoblasts, differentiated myotubes, and LPS-treated myotubes (0.2 mg/mL, 24 h). Scale bar = 100 µm. (**b**) Quantification of myotube width in control and LPS-treated groups ($n = 3$, $p = 0.0183$, Cohen's $d = 3.14$, 95% CI [1.537, 9.496]). (**c**) Representative fluorescence images of MitoTracker Red CMXRos-stained myoblasts, myotubes, and LPS-treated myotubes. Scale bar = 100 µm. (**d**) Quantification of MitoTracker fluorescence intensity relative to myoblasts ($n = 3$; myoblast vs. myotube, $p = 0.0003$, Cohen's $d = 9.63$, 95% CI [− 66.52, − 41.16]; myotube vs. myotube + LPS, $p = 0.009$, Cohen's $d = 3.87$, 95% CI [14.39, 55.00]). (**e**) Relative mRNA expression levels of MuRF-1 ($p = 0.0454$, Cohen's $d = 2.34$, 95% CI [− 0.8699, − 0.01472]) and Atrogin-1 ($p = 0.0494$, Cohen's $d = 2.28$, 95% CI [− 0.3060, − 0.0006591]) in control and LPS-treated myotubes assessed by RT-qPCR ($n = 3$). Data are presented as mean ± SD.

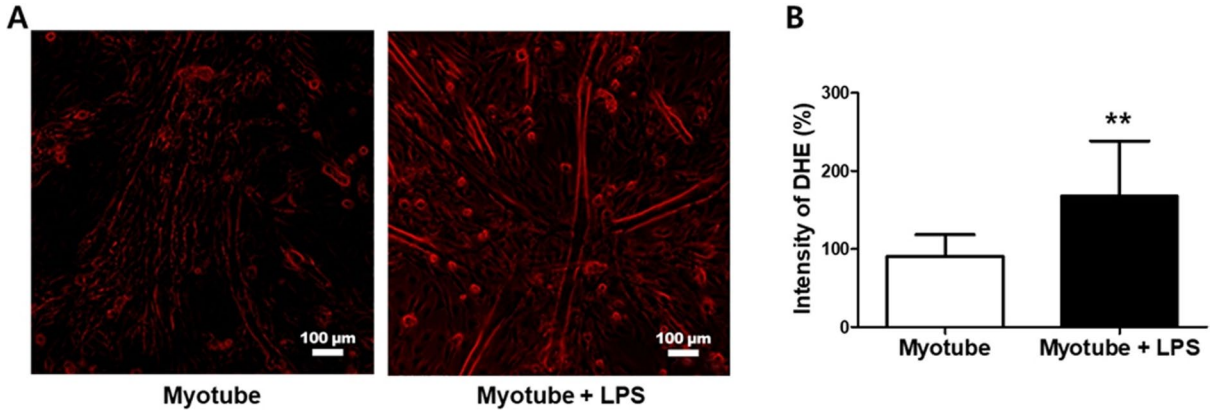


Fig. 3. Assessment of ROS levels in C2C12 myotubes using DHE fluorescence. (**a**) Representative fluorescence images of C2C12 myotubes stained with dihydroethidium (DHE; 20 µM, 30 min) in control and LPS-treated groups. Scale bar = 100 µm. (**b**) Quantification of DHE fluorescence intensity. LPS-treated myotubes exhibited increased fluorescence compared to controls, although the difference was not statistically significant ($n = 9$, $p = 0.0079$, Cohen's $d = 1.43$, 95% CI [− 131.1, − 23.29]). Data are presented as mean ± standard deviation (SD).

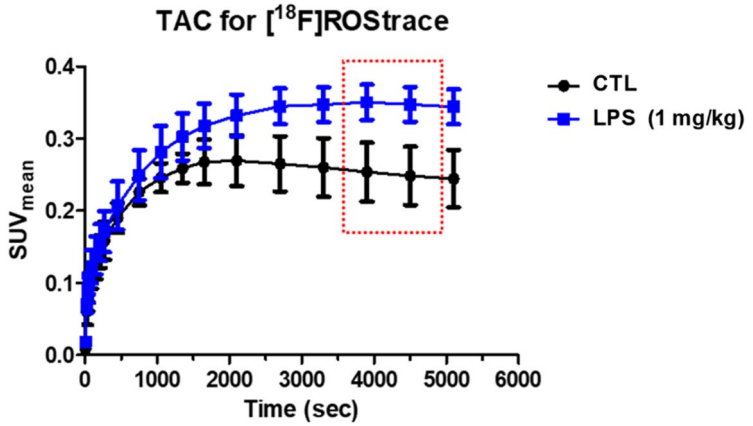


Fig. 4. Time acticity curve (TAC) of [^{18}F]ROStrace in the hindlimb muscle of control and LPS-treated mice. Dynamic PET imaging was performed for 90 min following [^{18}F]ROStrace injection (1 mg/kg LPS; $n = 3$ per group). TACs were derived from regions of interest in hindlimb muscles. The [^{18}F]ROStrace uptake reached a plateau phase approximately 60–80 min post-injection (highlighted in red box).

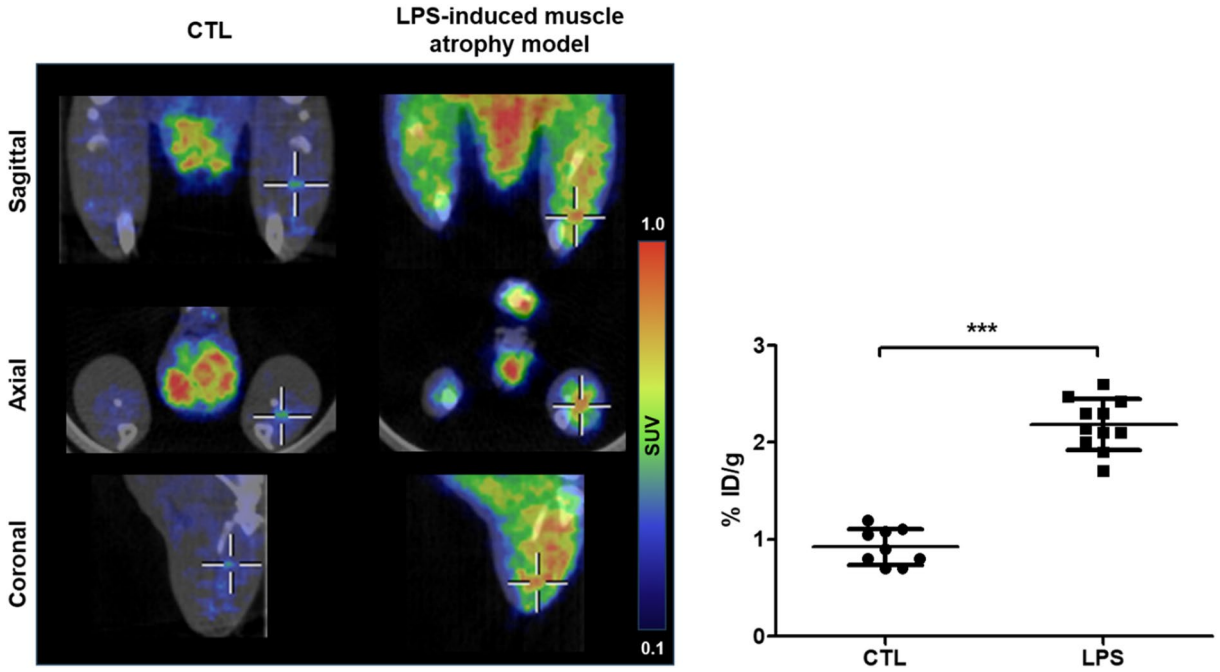


Fig. 5. [^{18}F]ROStrace uptake in the hindlimb muscles of LPS-induced oxidative stress in skeletal muscle mice. Representative PET/CT images show [^{18}F]ROStrace accumulation in the hindlimb regions of control (CTL) and LPS-treated mice (LPS, 5 mg/kg, 24 h post-injection). Sagittal, axial, and coronal views are displayed. Quantitative analysis of tracer uptake revealed significantly elevated uptake in the LPS group (2.2 ± 0.3%ID/g, $n = 11$) compared to the CTL group (0.9 ± 0.2%ID/g, $n = 9$) ($p < 0.0001$, Cohen's $d = 5.41$, 95% CI [− 1.480, − 1.040]). Data are presented as mean ± standard deviation (SD).

To evaluate in vivo oxidative stress in skeletal muscle, PET/CT imaging was performed 24 h after intraperitoneal administration of LPS (5 mg/kg). [^{18}F]ROStrace was injected intravenously, and static PET/CT scans were acquired from 60 to 80 min post-injection. Quantitative analysis of tracer uptake in the hindlimb muscles revealed a significantly higher %ID/g in the LPS-treated group (2.2 ± 0.3%ID/g, $n = 11$) compared to the control group (0.9 ± 0.2%ID/g, $n = 9$), indicating elevated ROS levels in the LPS-induced oxidative stress model (Fig. 5).

Biological and structural validation of LPS-induced oxidative stress in an in vivo skeletal muscle model

To confirm the induction of oxidative stress and associated molecular responses in skeletal muscle following LPS treatment, biological and histological evaluations were performed after PET imaging. The weight of the excised hindlimb muscles was significantly reduced in the LPS-treated group (112.7 ± 5.8 mg, $n = 11$) compared to the control group (138.4 ± 12.9 mg, $n = 9$) (Fig. 6A). At the molecular level, real-time RT-qPCR analysis revealed markedly elevated expression of muscle atrophy-related genes in the LPS group. MuRF-1 expression increased by approximately 13-fold (1.7 ± 1.2 vs. 22.2 ± 7.0), and Atrogin-1 expression increased by about 10-fold (1.5 ± 1.1 vs. 14.8 ± 4.5) compared to the control group ($n = 4$ per group, $p < 0.01$ for both; Fig. 6B-C). Histological examination using hematoxylin and eosin staining showed structural alterations in the muscle fibers of LPS-treated mice (Fig. 6D). Quantitative analysis of muscle fiber cross-sectional area (CSA) demonstrated a significant reduction in the LPS group (1804.3 ± 121.8 μm^2) compared to the control group (2659.6 ± 278.6 μm^2), consistent with atrophic muscle morphology ($n = 3$ per group; Fig. 6E).

Validation of ROS accumulation in muscle tissue using DHE fluorescence

To verify whether [^{18}F]ROStrace uptake reflected in vivo ROS levels, dihydroethidium (DHE) fluorescence imaging was performed on muscle tissues following PET imaging. Mice received intravenous injections of DHE (5 mg/kg), and hindlimb muscles were harvested 1 h later. The samples were rapidly frozen in isopentane cooled with liquid nitrogen, cryosectioned at 10 μm thickness at −20 °C, and analyzed using fluorescence microscopy (Fig. 7A). Quantitative analysis of DHE fluorescence intensity revealed a significantly higher signal in the LPS-treated group compared to controls (246.8 ± 12.3% vs. 100.0 ± 27.0%, $n = 3$, $p = 0.001$; Fig. 7B), consistent with the ROS distribution observed via [^{18}F]ROStrace PET imaging.

Discussion

This study aimed to evaluate [^{18}F]ROStrace PET as a redox-sensitive imaging probe for detecting ROS generation in skeletal muscle under inflammatory conditions known to contribute to atrophic changes. Our findings demonstrate that [^{18}F]ROStrace enables direct, in vivo visualization of ROS generation, while complementary biological assays (MuRF-1, Atrogin-1, MitoTracker, and DHE) were used to contextually validate the imaging signal rather than to define atrophy itself[27].

In vitro, LPS-treated C2C12 myotubes exhibited significantly higher uptake of [^{18}F]ROStrace compared to controls, consistent with an increase in intracellular ROS levels. This elevated uptake was attenuated by pretreatment with the ROS scavenger NAC, whereas treatment with PL, a known ROS enhancer, further increased [^{18}F]ROStrace uptake, supporting the tracer's redox sensitivity. Furthermore, mitochondrial membrane potential was reduced in LPS-treated myotubes, as indicated by diminished MitoTracker fluorescence, and the mRNA

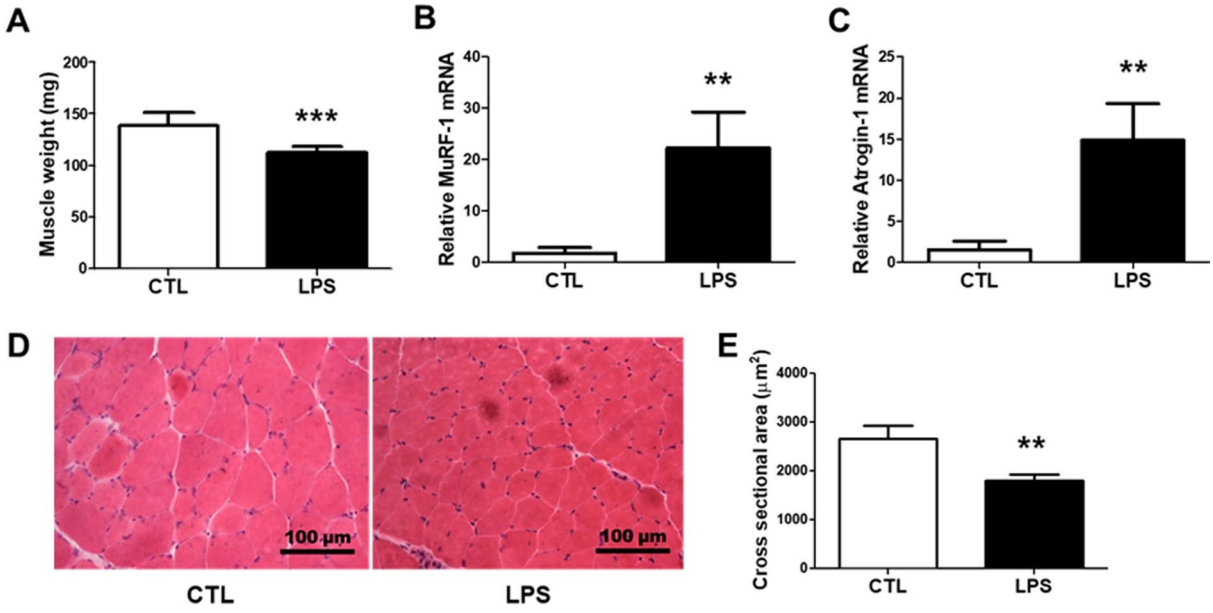


Fig. 6. Biological and structural responses to LPS-induced oxidative stress in an in vivo skeletal muscle model. (**a**) Hindlimb muscle weight in control ($n = 9$) and LPS-treated mice ($n = 11$) ($p < 0.0001$, Cohen's $d = 2.67$, 95% CI [16.64, 34.84]). (**b**, **c**) mRNA expression levels of MuRF-1 ($p = 0.0012$, Cohen's $d = 4.08$, 95% CI [−29.23, −11.82]) and Atrogin-1 ($p = 0.0011$, Cohen's $d = 4.12$, 95% CI [−18.99, −7.748]) in muscle tissue from each group assessed by RT-qPCR ($n = 4$ per group). (**d**) Representative H&E-stained images of muscle sections showing muscle fiber morphology (scale bar = 100 μm; $n = 3$ per group). (**e**) Quantification of muscle fiber cross-sectional area (CSA) between control and LPS-treated groups ($p = 0.0082$, Cohen's $d = 3.98$, 95% CI [368.0, 1343]). Data are presented as mean ± standard deviation (SD).

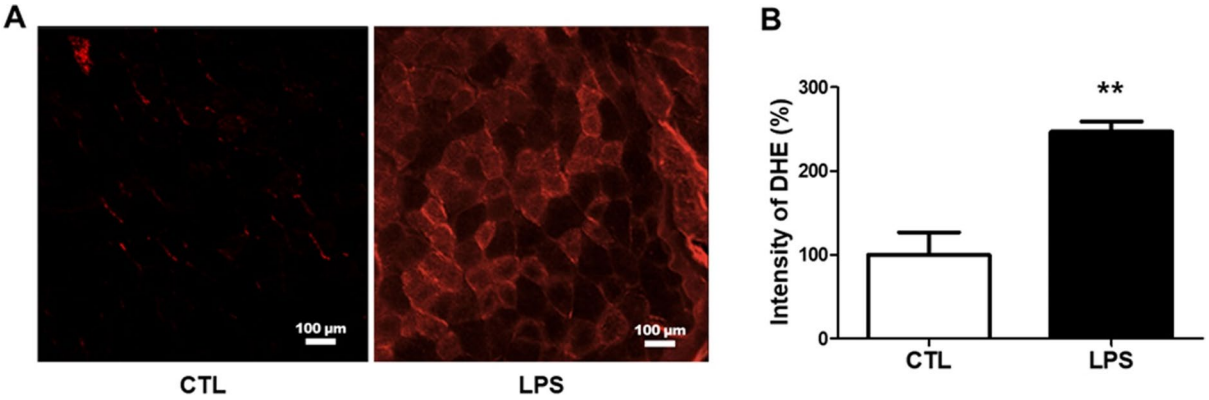


Fig. 7. Assessment of ROS levels in an in vivo skeletal muscle model of LPS-induced oxidative stress using DHE fluorescence. (**a**) Representative fluorescence images of hindlimb muscle sections stained with DHE (5 mg/kg, 1 h post-injection) in control and LPS-induced muscle atrophic mice. Scale bar = 100 μm. (**b**) Quantification of DHE fluorescence intensity revealed significantly increased ROS levels in the LPS-treated group (246.8 ± 12.3%) compared to controls (100.0 ± 27.0%) ($n = 3$, $p = 0.001$, Cohen's $d = 7.00$, 95% CI [-194.4, -99.26]). Data are expressed as mean ± standard deviation (SD).

levels of atrophy-related genes MuRF-1 and Atrogin-1 were markedly elevated. These findings are consistent with previous studies showing that oxidative stress contributes to muscle wasting through mitochondrial dysfunction and proteasome-mediated protein degradation[8,9,20,31,32]. In this study, MitoTracker Red CMXRos staining was used to assess mitochondrial membrane potential (ΔΨm) as a supportive indicator of oxidative stress, rather than a direct measure of mitochondrial bioenergetic function. A reduction in ΔΨm reflects early alterations in mitochondrial homeostasis and redox balance that may accompany oxidative stress–induced signaling cascades, but it cannot independently confirm mitochondrial dysfunction or atrophic progression. Our intent was therefore to use ΔΨm changes to complement other molecular readouts—such as MuRF-1, Atrogin-1, and DHE fluorescence—to establish a consistent oxidative phenotype under LPS-induced stress conditions.

We also used DHE staining instead of MitoSOX to assess ROS levels because the chemical backbone of DHE shares structural similarity with [^{18}F]ROStrace (DHE derivative). This provides a more direct validation of the tracer's redox reactivity and allows correlation between fluorescence-based ROS detection and PET imaging results. While MitoSOX specifically detects mitochondrial superoxide, [^{18}F]ROStrace primarily reflects total cellular ROS, including both mitochondrial and cytosolic sources. Therefore, DHE was considered more appropriate for validating the tracer's overall redox sensitivity in this study.

Importantly, while oxidative stress is mechanistically linked to atrophic signaling, the present study focuses on imaging ROS accumulation rather than quantifying structural muscle loss. The observed alterations in mitochondrial potential and atrophy-related genes therefore serve as biological correlates confirming that [^{18}F]ROStrace uptake reflects redox imbalance within muscle cells.

In vivo, [^{18}F]ROStrace PET/CT imaging revealed significantly increased tracer accumulation in the hindlimb muscles of LPS-induced atrophic mice compared to controls. This increased uptake was accompanied by a reduction in muscle mass, enlargement of muscle fiber cross-sectional area (CSA), and elevated expression of MuRF-1 and Atrogin-1, as confirmed by histological analysis and RT-qPCR. The pattern of [^{18}F]ROStrace uptake also mirrored the DHE fluorescence data in both in vitro and in vivo settings, further supporting the tracer's specificity for ROS detection and its utility as a redox imaging biomarker.

Notably, compared with previously reported ROS-targeted probes, [^{18}F]ROStrace offers several distinct advantages. Most existing radiotracers targeting oxidative stress either suffer from low in vivo stability or lack sufficient sensitivity to transient ROS fluctuations. [^{18}F]ROStrace, a fluorinated derivative of dihydroethidium (DHE), combines the high redox reactivity of DHE with favorable pharmacokinetics, enabling real-time, noninvasive quantification of total cellular ROS. Furthermore, current diagnostic approaches for muscle wasting—such as biopsy, MRI, and CT—are limited in their ability to assess dynamic biochemical changes. Biopsy is invasive and unsuitable for longitudinal evaluation, whereas MRI and CT primarily depict structural alterations without providing molecular insight into oxidative stress or proteolytic activity. In contrast, [^{18}F]ROStrace enables noninvasive visualization of reactive oxygen species (ROS) generation, providing a molecular biomarker of early pathological processes preceding overt tissue loss. Because muscle atrophy arises from multiple converging mechanisms—including oxidative stress, inflammation, and proteostasis imbalance—[^{18}F]ROStrace could contribute not only to mechanism-based diagnosis but also to the development and evaluation of targeted therapeutics.

Despite these promising findings, several limitations should be acknowledged. First, this study utilized an acute systemic inflammation model of LPS-induced oxidative stress in skeletal muscle, which may not fully represent chronic or progressive atrophic processes such as those observed in conditions such as sarcopenia, denervation, disuse, or neurogenic atrophy[6]. The sensitivity of [^{18}F]ROStrace under low-grade or early-stage oxidative stress conditions therefore remains to be evaluated. Second, the biodistribution and pharmacokinetics of [^{18}F]ROStrace in skeletal muscle may be influenced by factors such as regional perfusion, local metabolism,

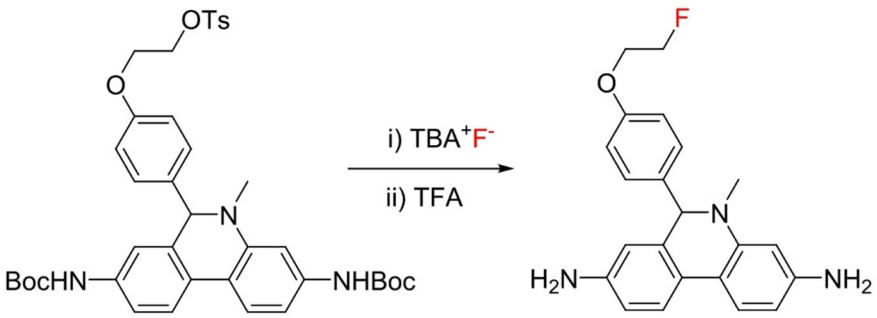


Fig. 8. Synthetic procedure of [^{18}F]ROStrace.

and systemic inflammatory status, which were not controlled or dissected in this study. Although a non-specific perfusion tracer was not used, quantification was performed using small, vessel-free VOIs and during the steady-state phase (60–80 min post-injection), when transient perfusion effects and blood radioactivity fluctuations are expected to be minimal. Arterial blood sampling was also not performed, and thus SUV_{mean} values were not corrected for blood tracer concentrations. While this may introduce some variability related to systemic clearance, the steady-state analysis likely mitigated major differences in blood activity. Nonetheless, this limitation should be considered when interpreting the quantitative data, and future studies incorporating blood sampling or image-derived input functions will improve kinetic accuracy.

Third, although [^{18}F]ROStrace PET and DHE fluorescence provided consistent evidence of superoxide accumulation, both approaches reflect total cellular ROS rather than compartment-specific sources. Because [^{18}F]ROStrace is a DHE-derived tracer, DHE staining was chosen to ensure a direct methodological correlation with PET imaging. Future studies employing mitochondrial-specific probes such as MitoSOX will further clarify the contribution of mitochondrial versus cytosolic ROS to the [^{18}F]ROStrace signal and refine the interpretation of redox dynamics in skeletal muscle.

Finally, future longitudinal studies in alternative models—such as age-related sarcopenia, immobilization, and neurodegenerative muscle wasting—combined with functional assessments of muscle performance, will be important to establish the diagnostic and therapeutic potential of [^{18}F]ROStrace PET for evaluating oxidative stress–related muscle pathology.

Conclusion

This study provides the first evidence that [^{18}F]ROStrace PET can noninvasively visualize ROS accumulation as a molecular indicator of oxidative stress in skeletal muscle, offering a redox-specific imaging approach that complements, rather than replaces, structural or atrophy-related assessments. The [^{18}F]ROStrace uptake showed a possible association with molecular markers of muscle degradation, such as MuRF-1 and Atrogin-1, and with structural changes in both in vitro and in vivo models, supporting its relevance as a redox-sensitive imaging tool. Although further validation across diverse models—including those driven by aging, disuse, or neurogenic mechanisms—is warranted, our findings highlight the potential of [^{18}F]ROStrace PET/CT to enhance the mechanistic understanding and diagnostic assessment of oxidative stress in muscle wasting. Moreover, integrating this imaging modality with therapeutic interventions targeting redox imbalance may provide valuable insights into treatment efficacy and disease progression in oxidative stress–related muscle pathology.

Materials and methods

Synthesis of [^{18}F]ROStrace

[^{18}F]ROStrace was synthesized from the tosylate precursor (2-(4-(3,8-bis((*tert*-butoxycarbonyl)amino)-5-methyl-5,6-dihydrophenanthridin-6-yl)phenoxy)ethyl 4-methylbenzenesulfonate) by nucleophilic aliphatic substitution with fluorine-18, as previously described with slight modifications as shown in Fig. 8[27,33]. Briefly, fluorine-18 in O-18 enriched water (98%) was extracted on preactivated Sep-Pak Light Plus QMA carbonate cartridge (ethanol 10 mL and water for injection 10 mL; Waters, Milford, MA, USA) by 40% wt% tetrabutylammonium bicarbonate ($TBAHCO_3$) dissolved in 1 mL of methanol into the 4 mL reaction vial. The eluate was azeotropically evaporated twice with acetonitrile (CH_3CN, 0.4 mL) under a stream of nitrogen at 100 °C to remove residual water. Subsequently, 2.7 mg of the ROS-tracer precursor in CH_3CN: t-BuOH (0.45:0.05 mL, 9:1, v/v) was added to the dried [^{18}F]TBA^+F^- complex, and the reaction mixture was heated at 100 °C for 15 min. For deprotection, 0.1 mL of trifluoroacetic acid (TFA) was added, and the mixture was incubated at 80 °C for an additional 15 min. After cooled to room temperature, the mixture was neutralized with 1.2 mL of 1 N NaOH and diluted with 10 mL of deionized water. The solution was loaded onto a Sep-Pak Plus tC18 cartridge (Waters), washed with 5 mL of water, and the product was eluted with 2 mL of 80% (v/v) CH_3CN: H_2O. The eluate was diluted with 1 mL of water, passed through a 0.45 μm UHP-HPLC filter and purified by semi-preparative radio-HPLC (Waters, Xterra RP18; mobile phase: 40% CH_3CN:0.1 M ammonium formate; flow rate: 4 mL/min; UV-254 nm and gamma detector). [^{18}F]ROStrace was collected at a retention time of approximately 21 min, diluted with 17 mL of water, and reloaded onto a tC18 cartridge. For the final formulation, desire [^{18}F] ROStrace was eluted with 90% EtOH: H_2O, treated with sodium borohydride ($NaBH_4$, 1 mg), and heated at 65

°C for 20 min. Ascorbic acid (5 mg) was then added to stabilize the product. The final [^{18}F]ROStrace solution was diluted in either saline or culture medium for subsequent in vivo or in vitro applications.

Cell culture and differentiation

The mouse skeletal muscle myoblast cell line C2C12 (ATCC, Manassas, VA, USA) was cultured in growth medium (GM) consisting of high-glucose Dulbecco's Modified Eagle's Medium (DMEM; WELGENE, Gyeongsan, Korea) supplemented with 10% fetal bovine serum (FBS; Gibco, Grand Island, NY, USA), 1% penicillin–streptomycin (Gibco), and 0.05% Normocin™ (InvivoGen, San Diego, CA, USA). Cells were maintained at 37 °C in a humidified atmosphere containing 5% CO_2. To preserve differentiation capacity, cells were passaged at 50% confluency and only early-passage cells (passage number < 20) were used. For myogenic differentiation, C2C12 myoblasts were seeded in 6-well plates and allowed to reach 90–100% confluency. After 24 h, the GM was replaced with differentiation medium (DM), composed of DMEM supplemented with 2% horse serum (Gibco), to replace FBS[34]. Cells were maintained in DM for at least 5 days, with the medium changed every other day. Morphological differentiation into multinucleated myotubes was confirmed by daily microscopic observation. To induce oxidative stress and early atrophy-related signaling in vitro, differentiated myotubes were treated with 0.2 mg/mL lipopolysaccharide (LPS; Sigma-Aldrich, St. Louis, MO, USA) in DM. LPS-treated cells were incubated for 24 h prior to downstream analyses[35,36]. Where applicable, additional treatment groups such as antioxidant or oxidative enhancer conditions were included in the same culture format for subsequent cellular uptake experiments[37].

Animals

All animal procedures were approved by the Institutional Animal Care and Use Committee (IACUC) of Ewha Womans University College of Medicine (Approval No. EWHA MEDIACUC 23-031-1) and were conducted in accordance with institutional and national guidelines, ARRIVE recommendations, and all relevant regulations. Male C57BL/6 N mice (7 weeks old) were obtained from Orient Bio (Seongnam, Korea) and acclimatized for one week prior to experimentation. Mice were housed in a temperature-controlled environment (24 °C, 40% humidity) under a 12-hour light/dark cycle, with free access to standard chow and water. Animals were randomly assigned to either the control group (CTL, $n = 12$) or the LPS-induced oxidative stress in skeletal muscle group (LPS, $n = 14$). Within each group, subsets of mice were allocated for dynamic PET scans (90 min) or static scans (60–80 min post-injection). For the dynamic scan, both CTL and LPS groups included three mice ($n = 3$ per group); LPS-treated mice for this scan received 1 mg/kg of LPS (in 0.2 mL saline) via intraperitoneal injection. For the static scan, the remaining mice (CTL, $n = 9$; LPS, $n = 11$) were used, with LPS-treated mice receiving 5 mg/kg of LPS in the same volume. Before imaging, mice were anesthetized with 5% isoflurane for induction and maintained on 1–2% isoflurane in a 7:3 N_2/O_2 mixture. PET/CT scans were acquired 24 h after LPS injection in a dedicated small animal PET/CT (NanoPET/CT, Bioscan Inc., Washington, DC, USA). After imaging, animals were deeply anesthetized with isoflurane (2.5% in a 7:3 N_2/O_2 mixture) and euthanized by transcardiac perfusion with 1× PBS, consistent with the AVMA Guidelines for the Euthanasia of Animals (2020). The hindlimb muscles were then harvested, weighed, and processed for downstream analyses. For molecular assays, tissues were stored at − 80 °C (CTL and LPS, $n = 4$ per group). For histological evaluation, muscle samples were embedded in isopentane precooled in liquid nitrogen and stored appropriately (CTL and LPS, $n = 3$ per group).

Cell morphology observation and fluorescence imaging

The morphology of C2C12 myoblasts and differentiated myotubes was observed using an optical microscope (CKX53, Olympus, Tokyo, Japan). To assess morphological changes induced by LPS treatment, myotube width was measured at three distinct points along each fiber. Measurements were performed on multiple myotubes from three independent experiments. To evaluate mitochondrial membrane potential, cells were incubated with MitoTracker™ Red CMXRos (Invitrogen, Carlsbad, CA, USA) at a final concentration of 200 nM in either growth medium (GM) or differentiation medium (DM). For assessment of intracellular ROS levels, cells cultured in DM were treated with dihydroethidium (DHE; MedChemExpress, Monmouth Junction, NJ, USA) at a final concentration of 20 μM. After staining, cells were incubated in the dark for 30 min at 37 °C in a 5% CO_2 atmosphere and imaged using a fluorescence microscope (Ti2-U, Nikon, Tokyo, Japan). Quantification of myotube width and fluorescence intensity was performed using ImageJ software (version 1.53t, NIH, USA).

Cell uptake of [^{18}F]ROStrace in C2C12 myotube

C2C12 myotubes were cultured in 6-well plates and divided into four experimental groups: untreated myotubes (Myotube, $n = 5$), LPS-treated myotubes (Myotube + LPS, $n = 5$), NAC-pretreated myotubes (Myotube + NAC + LPS, $n = 5$), and piperlongumine-pretreated myotubes (Myotube + PL + LPS, $n = 5$). To induce oxidative stress, 0.2 mg/mL of LPS was added to the differentiation medium, and cells were incubated for 24 h. To validate the responsiveness of [^{18}F]ROStrace to changes in oxidative stress levels, *N*-acetylcysteine (NAC; 3 mM), a ROS scavenger, was added 1 h prior to LPS exposure, while piperlongumine (PL; 10 μM), an enhancer of oxidative stress, was added 3 h before LPS treatment[34]. Both reagents were maintained in the medium throughout the LPS treatment period. After 24 h of LPS incubation, each well was incubated with differentiation medium containing [^{18}F]ROStrace at a final activity of ~ 10 μCi per well. Each experimental group was further subdivided into four time-point subgroups and incubated with [^{18}F]ROStrace for 10, 30, 60, and 120 min, respectively, at 37 °C in a 5% CO_2 incubator. Following incubation, cells were washed with PBS, harvested via trypsinization, and transferred into pre-weighed tubes. The radioactivity of each sample was measured using a gamma counter (Wizard^2 2480, PerkinElmer, Waltham, MA, USA), and counts were corrected for the decay of fluorine-18.

Standard reference samples of [^{18}F]ROStrace were also measured in parallel for accurate quantification. The uptake of [^{18}F]ROStrace was expressed as the percentage of the injected dose (%ID) per well.

microPET/CT imaging

All mice were anesthetized with 2.5% isoflurane and administered a single intravenous dose of [^{18}F]ROStrace (7.0 ± 0.7 MBq). PET/CT imaging (NanoPET/CT, Mediso Medical Imaging Systems, Budapest, Hungary) was performed to assess tracer uptake in control (CTL, $n = 12$) and LPS-induced oxidative stress in skeletal muscle (LPS, $n = 14$) groups. Of these, mice from each group ($n = 3$ per group) were used for dynamic PET scans lasting 90 min immediately following tracer injection. The remaining mice (CTL, $n = 9$; LPS, $n = 11$) underwent static PET imaging from 60 to 80 min post-injection, corresponding to the expected equilibrium phase of [^{18}F] ROStrace biodistribution. For static imaging, mice were allowed to recover and remain conscious for 60 min after tracer administration, then re-anesthetized with 2.5% isoflurane and subjected to PET/CT imaging for 20 min. CT scans were acquired for attenuation correction and anatomical localization. PET images were reconstructed using a three-dimensional Adjoint Monte Carlo method with corrections for scattering and random events. Quantitative analysis was performed by manually drawing volumes of interest (VOIs) over hindlimb muscle regions in the fused PET/CT images, using a 2.0-mm radius region of interest delineated by the intensely visualized region in the summed image. Tracer uptake was expressed as the percentage of the injected dose per gram of tissue (%ID/g), calculated by normalizing PET signal intensity to the injected activity and the body weight of each mouse after attenuation correction. All PET/CT data were processed and analyzed using InterView Fusion software (version 3.03.089.00; Mediso Medical Imaging Systems, Budapest, Hungary).

Histological analysis

Following PET imaging, mice in both CTL and LPS-treated groups were further subdivided according to the intended analysis. For dihydroethidium (DHE) fluorescence imaging, mice ($n = 3$ per group) were intravenously injected with DHE at a dose of 5 mg/kg. One hour post-injection, hindlimb muscles were excised and rapidly frozen in isopentane pre-cooled with liquid nitrogen. Cryosections were prepared at a thickness of 10 μm using a cryostat maintained at − 20 °C. Fluorescence images were acquired using a fluorescence microscope (Ti2-U, Nikon), and quantitative analysis of fluorescence intensity was performed using ImageJ software (version 1.53t, NIH, USA). For hematoxylin and eosin (H&E) staining, hindlimb muscle tissues were also rapidly frozen in isopentane and cryosectioned at a thickness of 10 μm. Sections were stained using a commercial H&E staining kit according to the manufacturer's protocol, and images were captured using a light microscope equipped with an image analysis system (BX50, Olympus, Tokyo, Japan). The cross-sectional area (CSA) of individual muscle fibers was measured using ImageJ software.

Real-time quantitative PCR

Total RNA was extracted from mouse hindlimb muscle tissues or differentiated C2C12 myotubes using the RNeasy Plus Mini Kit (QIAGEN, Hilden, Germany), following the manufacturer's instructions. First-strand cDNA synthesis was performed using the SuperScript™ III First-Strand Synthesis System (Invitrogen, Carlsbad, CA, USA). Quantitative real-time PCR was conducted on the QuantStudio 3 Real-Time PCR System (Applied Biosystems, MA, USA). The following gene-specific primers were used: MuRF-1: forward 5′-CTT CCT CTC AAG TGC CAA GCA-3′, reverse 5′-GTG TTC TAA GTC CAG AGT AAA GTA GTC CAT-3′; Atrogin-1: forward 5′-GAC CGG CTA CTG TGG AAG AG-3′, reverse 5′-CCA GGA GAG AAT GTG GCA GT-3′; GAPDH (reference gene): forward 5′-AAG GTC ATC CCA GAG CTG AA-3′, reverse 5′-AGG AGA CAA CCT GGT CCT-3′). The thermal cycling conditions were as follows: an initial pre-incubation at 50 °C for 2 min and 95 °C for 2 min, followed by 40 cycles of amplification consisting of denaturation at 95 °C for 15 s and annealing/extension at 60 °C for 1 min. Gene expression levels of MuRF-1 and Atrogin-1 were normalized to GAPDH expression and calculated using the comparative $2^{-\Delta\Delta CT}$ method relative to the average values of the control group.

Statistical analyses

All statistical analyses were performed using GraphPad Prism software (version 5.0; GraphPad Software, San Diego, CA, USA). Data normality and equality of variances were separately tested. Normality was assessed using the Shapiro–Wilk test to confirm that the data followed a normal distribution, and equality of variances between the two groups was evaluated using an F-test. When both assumptions were satisfied, the Student's t-test was applied for comparison. A p-value of less than 0.05 was considered statistically significant. Data are presented as mean ± standard deviation (SD). In the present experiment, no data points were excluded from analysis. The number of replicates (n) reported for each experiment represents biological replicates (independent cell cultures or individual animals).

Data availability

The datasets used and analyzed during the current study are available from the corresponding author on reasonable request.

Received: 9 June 2025; Accepted: 6 January 2026
Published online: 09 January 2026

References

1. Kamei, Y., Hatazawa, Y., Uchitomi, R., Yoshimura, R. & Miura, S. Regulation of skeletal muscle function by amino acids. *Nutrients* **12**, 261 (2020).

2. Yamakawa, H., Kusumoto, D., Hashimoto, H. & Yuasa, S. Stem cell aging in skeletal muscle regeneration and disease. *Int. J. Mol. Sci.* **21**, 1830 (2020).
3. Galpin, A. J. et al. Human skeletal muscle fiber type specific protein content. *Anal. Biochem.* **425**, 175–182 (2012).
4. Hargreaves, M. & Spriet, L. L. Exercise metabolism: fuels for the fire. *Cold Spring Harb Perspect. Med.* **8**, a029744 (2018).
5. Chen, K. et al. Forkhead box O signaling pathway in skeletal muscle atrophy. *Am. J. Pathol.* **192**, 1648–1657 (2022).
6. Yin, L. et al. Skeletal muscle atrophy: from mechanisms to treatments. *Pharmacol. Res.* **172**, 105807 (2021).
7. Yoshihara, I., Kondo, Y., Okamoto, K. & Tanaka, H. Sepsis-associated muscle wasting: A comprehensive review from bench to bedside. *Int. J. Mol. Sci.* **24**, 5040 (2023).
8. Kamal, K. Y. & Trombetta-Lima, M. Mechanotransduction and skeletal muscle atrophy: the interplay between focal adhesions and oxidative stress. *Int. J. Mol. Sci.* **26**, 2802 (2025).
9. Park, S. M. et al. Feasibility of [^{18}F]fluorocholine PET for evaluating skeletal muscle atrophy in a starved rat model. *Diagnostics* **12**, 1274 (2022).
10. Eshima, H. et al. Neutralizing mitochondrial ROS does not rescue muscle atrophy induced by hindlimb unloading in female mice. *J. Appl. Physiol. (1985).* **129**, 124–132 (2020).
11. Yang, B. et al. IL-6 Deficiency attenuates skeletal muscle atrophy by inhibiting mitochondrial ROS production through the upregulation of PGC-1α in septic mice. *Oxid. Med. Cell Longev.* 9148246 (2022). (2022).
12. Hiensch, A. E. et al. Doxorubicin-induced skeletal muscle atrophy: elucidating the underlying molecular pathways. *Acta Physiol.* **229**, e13400 (2020).
13. Ninfali, C. et al. The adaptive antioxidant response during fasting-induced muscle atrophy is oppositely regulated by ZEB1 and ZEB2. *Proc. Natl. Acad. Sci. USA* 120, e2301120120 (2023).
14. Ryu, Y. et al. Sabinene prevents skeletal muscle atrophy by inhibiting the MAPK-MuRF-1 pathway in rats. *Int. J. Mol. Sci.* **20**, 4955 (2019).
15. Le, N. H. et al. Quercetin protects against obesity-induced skeletal muscle inflammation and atrophy. *Mediators Inflamm.* 834294 (2014). (2014).
16. Gumucio, J. P. & Mendias, C. L. Atrogin-1, MuRF-1, and sarcopenia. *Endocrine* **43**, 12–21 (2013).
17. Park, J. Y. et al. Radiopharmaceuticals for skeletal muscle PET imaging. *Int. J. Mol. Sci.* **25**, 4860 (2024).
18. Park, J. Y. et al. Innovations in nuclear medicine imaging for reactive oxygen species: applications and radiopharmaceuticals. *Antioxidants* **13**, 1254 (2024).
19. Sivapackiam, J. et al. Preclinical validation of a novel PET tracer for non-invasive imaging of oxidative stress *in vivo*. *Redox Biol.* **37**, 101690 (2020). Galuminox.
20. Chen, X. et al. Mitochondrial dysfunction: roles in skeletal muscle atrophy. *J. Transl Med.* **21**, 503 (2023).
21. Zhang, H. et al. Oxidative stress: roles in skeletal muscle atrophy. *Biochem. Pharmacol.* **214**, 115664 (2023).
22. Heurling, K. et al. Quantitative positron emission tomography in brain research. *Brain Res.* **1670**, 220–234 (2017).
23. Nakase, J. et al. Whole body muscle activity during the FIFA 11$^+$ program evaluated by positron emission tomography. *PLoS ONE.* **8**, e73898 (2013).
24. Jackson, R. S., Schlarman, T. C., Hubble, W. L. & Osman, M. M. Prevalence and patterns of physiologic muscle uptake detected with whole-body [^{18}F]FDG PET. *J. Nucl. Med. Technol.* **34**, 29–33 (2006).
25. Kawada, K., Iwamoto, M. & Sakai, Y. Mechanisms underlying [^{18}F]fluorodeoxyglucose accumulation in colorectal cancer. *World J. Radiol.* **8**, 880–886 (2016).
26. Heinonen, I. et al. Increasing exercise intensity reduces heterogeneity of glucose uptake in human skeletal muscles. *PLoS ONE.* **7**, e52191 (2012).
27. Hou, C. et al. Development of a positron emission tomography Radiotracer for imaging elevated levels of superoxide in neuroinflammation. *ACS Chem. Neurosci.* **9**, 578–586 (2018).
28. Hsieh, C. J. et al. Correction: [^{18}F]ROStrace detects oxidative stress *in vivo* and predicts progression of alzheimer's disease pathology in APP/PS1 mice. *EJNMMI Res.* **12**, 43 (2023).
29. Weng, C. C. et al. Correlation analysis of [^{18}F]ROStrace using ex vivo autoradiography and dihydroethidium fluorescent imaging in lipopolysaccharide-treated animals. *Biochem. Biophys. Res. Commun.* **516**, 397–401 (2019).
30. Zhu, Y. et al. PET imaging with [^{18}F]ROStrace detects oxidative stress and predicts parkinson's disease progression in mice. *Antioxidants* **13**, 1226 (2024).
31. Dai, H. et al. Astragaloside IV alleviates sepsis-induced muscle atrophy by inhibiting the TGF-β1/Smad signaling pathway. *Int. Immunopharmacol.* **115**, 109640 (2023).
32. Chen, R. et al. N-Acetylcysteine attenuates sepsis-induced muscle atrophy by downregulating Endoplasmic reticulum stress. *Biomedicines* **12**, 902 (2024).
33. Chu, W. et al. Development of a PET Radiotracer for non-invasive imaging of the reactive oxygen species, superoxide, *in vivo*. *Org. Biomol. Chem.* **12**, 4421–4431 (2014).
34. De, Carlo, F. et al. Nonionizing radiation as a noninvasive strategy in regenerative medicine: the effect of Ca^{2+}-ICR on mouse skeletal muscle cell growth and differentiation. *Tissue Eng. Part. A.* **18**, 2248–2258 (2012).
35. Gallagher, E. et al. Positron emission tomography with [^{18}F]ROStrace reveals progressive elevations in oxidative stress in a mouse model of alpha-synucleinopathy. *Int. J. Mol. Sci.* **25**, 4943 (2024).
36. Chen, K. et al. Pseurotin a inhibits osteoclastogenesis and prevents ovariectomized-induced bone loss by suppressing reactive oxygen species. *Theranostics* **9**, 1634–1650 (2019).
37. Jin, H-O. et al. Piperlongumine induces cell death through ROS-mediated CHOP activation and potentiates TRAIL-induced cell death in breast cancer cells. *J. Cancer Res. Clin. Oncol.* **140**, 2039–2046 (2014).

Acknowledgements

We would like to thank to Won Chul Park for the support of chemical synthesis.

Author contributions

J.Y.P. and S.M.P. conducted the radiosynthesis of the described radiotracer, performed *in vitro* experiments, animal imaging and tissue characterization experiments, interpreted the data and wrote the initial draft of the manuscript. T.S.L. contributed to the development of methodologies for both *in vitro* and *in vivo* experiments. S.J.L. and S.J.O. assisted to the radiosyntheis of the radiotracer. H.J.Y., J.Y.K. and B.S.K. supported animal imaging and image analysis. B.S.M. supervised the overall project, contributed to the conception of the study, and participated in manuscript review and editing. All authors engaged in scientific discussion, contributed to the revision of the manuscript, and approved the final version of the manuscript.

Funding

This research was supported by grants from the Basic Science Research Program through the National Research

Foundation of Korea funded by the Ministry of Science and ICT (RS-2024-00339811, RS-2024-00449684, and 2021R1I1A1A01049147) and the Korea Health Technology R&D Project through the Korea Health Industry Development Institute funded by the Ministry of Health and Welfare (HR18C0016), Republic of Korea.

Declarations

Competing interests

The authors declare no competing interests.

Additional information

Correspondence and requests for materials should be addressed to B.S.K. or B.S.M.

Reprints and permissions information is available at www.nature.com/reprints.

Publisher's note Springer Nature remains neutral with regard to jurisdictional claims in published maps and institutional affiliations.

Open Access This article is licensed under a Creative Commons Attribution-NonCommercial-NoDerivatives 4.0 International License, which permits any non-commercial use, sharing, distribution and reproduction in any medium or format, as long as you give appropriate credit to the original author(s) and the source, provide a link to the Creative Commons licence, and indicate if you modified the licensed material. You do not have permission under this licence to share adapted material derived from this article or parts of it. The images or other third party material in this article are included in the article's Creative Commons licence, unless indicated otherwise in a credit line to the material. If material is not included in the article's Creative Commons licence and your intended use is not permitted by statutory regulation or exceeds the permitted use, you will need to obtain permission directly from the copyright holder. To view a copy of this licence, visit http://creativecommons.org/licenses/by-nc-nd/4.0/.

© The Author(s) 2026